Characterization of neonatal aortic cannula jet flow regimes for improved cardiopulmonary bypass

Prahlad G. Menon [a], Nikola Teslovich [a], Chia-Yuan Chen [a], Akif Undar [b], Kerem Pekkan [a,c,*]

[a] Department of Biomedical Engineering, Carnegie Mellon University, Pittsburgh, PA 15219, United States
[b] Penn State Milton S. Hershey Medical Center, Hershey, PA 17033, United States
[c] Department of Mechanical Engineering, Koç University, Istanbul, Turkiye

ABSTRACT

During pediatric and neonatal cardiopulmonary bypass (CPB), tiny aortic outflow cannulae (2–3 mm inner diameter), with micro-scale blood-wetting features transport relatively large blood volumes (0.3 to 1.0 L/min) resulting in high blood flow velocities (2 to 5 m/s). These severe flow conditions are likely to complement platelet activation, release pro-inflammatory cytokines, and further result in vascular and blood damage. Hemodynamically efficient aortic outflow cannulae are required to provide high blood volume flow rates at low exit force. In addition, optimal aortic insertion strategies are necessary in order to alleviate hemolytic risk, post-surgical neurological complications and developmental defects, by improving cerebral perfusion in the young patient. The methodology and results presented in this study serve as a baseline for design of superior aortic outflow cannulae. In this study, direct numerical simulation (DNS) computational fluid dynamics (CFD) was employed to delineate baseline hemodynamic performance of jet wakes emanating from microCT scanned state-of-the-art pediatric cannula tips in a cuboidal test rig operating at physiologically relevant laminar and turbulent Reynolds numbers (Re: 650–2150 , steady inflow). Qualitative and quantitative validation of CFD simulated device-specific jet wakes was established using time-resolved flow visualization and particle image velocimetry (PIV). For the standard end-hole cannula tip design, blood damage indices were further numerically assessed in a subject-specific cross-clamped neonatal aorta model for different cannula insertion configurations. Based on these results, a novel diffuser type cannula tip is proposed for improved jet flow-control, decreased blood damage and exit force and increased permissible flow rates. This study also suggests that surgically relevant cannula orientation parameters such as outflow angle and insertion depth may be important for improved hemodynamic performance. The jet flow design paradigm demonstrated in this study represents a philosophical shift towards cannula flow control enabling favorable pressure-drop versus outflow rate characteristics.

1. Introduction

In the US, approximately 1 in 100 children are born with a clinically significant congenital heart defect (CHD), representing 30,000 children each year in the United States and 1300,000 children worldwide. The palliative repair of these defects requires complex biventricular and univentricular surgical operations in newborns often smaller than 2 kg. A major component of these surgeries is the cardiopulmonary bypass (CPB) procedure which can potentially lead to neurological complications and developmental defects in young patients due to poor cerebral perfusion. Blood damage resulting from high blood flow velocities in the cannulated aorta is hypothesized to be another major problem

and severe flow conditions may result in platelet activation as well as vascular injury.

In comparison with adult aortic cannulae where the design focus is on reducing outflow velocities in order to prevent dislodging of atherosclerotic plaque on cannulated vessel (White et al., 2009), the primary design goal of pediatric and neonatal cannulae is different and more challenging. As an anecdotal example regarding outflow velocities, at 1 L/min, an 8FR (~2 mm inner diameter) pediatric cannula is likely to experience between 3 – 4 m/s peak inflow velocity (subject to variability in inner diameters), whereas the 24FR adult size cannula would have a jet velocity that is 3 times lower for the same Reynolds numbers (Re). Present literature has indicated biomechanical risks of aortic cannulation in adults (Kaufmann et al., 2009a, 2009b; Tokuda et al., 2008) but there are no studies to our knowledge that focus neonatal CPB cannulation. Our recent investigations have indicated the high hemolytic risk of standard aortic cannulae used in the setting of pediatric CPB procedures compared to adult cannulae and post intervention recovery

* Correspondence to: Department of Biomedical Engineering, Carnegie Mellon University, 700 Technology Drive, Pittsburgh, PA 15219, United States.
Tel.: +1 412 259 3031; fax: +1 404 268 9807.
E-mail addresses: kpekkan@andrew.cmu.edu, kpekkan@ku.edu.tr (K. Pekkan).
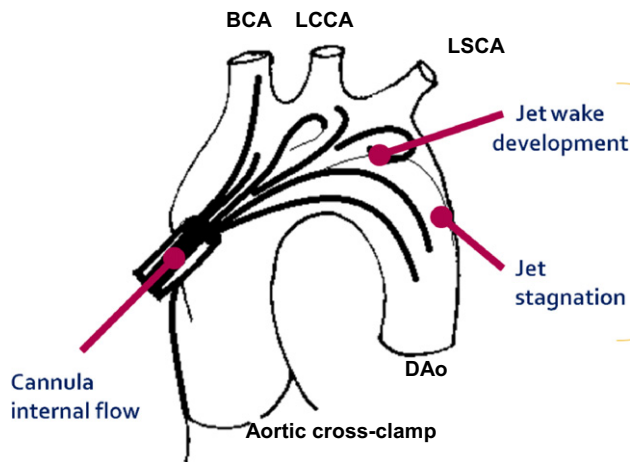
Fig. 1. Annotated illustration of major flow regimes of cannula hemodynamics, in a cross-clamped aortic arch. Each flow region requires a dedicated investigation. BCA: brachiocephalic artery; LCCA: left common carotid artery; LSCA: left subclavian artery; DAo: descending aorta.

has been reported to remain suboptimal (McElhinney et al., 2010; Pekkan et al., 2008; Wang et al., 2009). Therefore, there is a definitive need for engineering small yet hemodynamically efficient aortic outflow cannulae for neotatal and pediatric CPB procedures which can provide high blood volume flow rates but with low exit force and outflow velocity while minimizing recognized risks related to infection, bleeding, hemolysis and thromboembolism while improving cerebral perfusion during mechanical circulatory support.

The major flow regimes of interest during CPB are labeled in Fig. 1, for an illustrated cross-clamped aortic arch sketch. *The main focus of this project is to study hemodynamics in the jet wake of current state-of-the-art aortic cannula, and to document baseline blood damage indices, with specific attention to improving cannula tip design.* Jet-wake analysis is first performed in a confined cuboidal test rig for common cannula tips. Influence of cannulation in three-dimensional (3D) aortic arch geometry is further assessed using a patient-specific model. A novel diffuser-tipped cannula design is investigated as a potential improvement to standard end-hole and oblique cut tip designs from the standpoint of decreased blood damage and increased permissible flow rates.

Currently, the hydrodynamic behavior of neonatal cannulae are evaluated by basic pressure loss versus flow rate characteristics which are obtained from in-vitro experiments (De Wachter et al., 2002; Qiu et al., 2011) or with the M-number (Montoya et al., 1991). The latter is further applicable only to characterizing pressure–flow relationships of cannulae having regular internal diameters, for a given length. Therefore, a majority of cannula studies have focused on their design from the standpoint of blood flow rate and pressure drop across the cannula. This methodology neither furnishes information about the local fluid dynamics nor establishes the nature of the flow field in specific clinical conditions.

Device-specific cannula flow studies have been conducted to assess local hemodynamics using computational fluid dynamics (CFD) simulation inside rigid vessels (Grigioni et al., 2002). However such studies are limited to the regions that are closer to the cannula and unduly simplify the problem using planes of symmetry. Therefore, a truly 3D CFD numerical assessment of the fluid dynamics created by different outflow cannula tip designs can provide key information that both: (a) support the design of superior aortic cannulae; and (b) establish optimal clinical use parameters such as insertion depth and outflow angle, limiting risks of biomechanical origin. In the present study, high-resolution

3D CFD characterization of pediatric and neonatal cannula jet streams are conducted for the first time in the literature for device-specific evaluation of jet wake hemodynamic effects. The know-how reported in this study is essential to engineer cannula tips that can control jet wake fluid dynamics in the future.

2. Methods

Device specific jet flow CFD simulations were performed for microCT scanned 8FR cannulae: RMI FEM II -008-ATI (RMI), a standard end-hole cannula tip, and DLP Medtronic 77008 (DLP), an oblique cut end-hole cannula tip in a confined cuboidal test-rig (see Fig. 2 for sample microCT reconstructions). The extended set of cannula tips that are investigated in this study also included a novel 15° diffuser cannula tip design (15° half cone-angle) which was compared with current neonatal cannula designs. Additionally, time-resolved flow visualization experiments and particle image velocimetry (PIV) were conducted in an experimental in-vitro flow loop in order to experimentally validate CFD results. Jet-axial pressure-drop versus flow rate characteristics were measured experimentally in order to complement our numerical studies. Finally, since, the significance of intra-operative outflow cannula positioning (Osorio et al., 2011) in mitigating clinical stroke-risk (1–3% risk) cannot be discounted (Andropoulos et al., 2010), the utility of the CFD technique is extended to derive surgically relevant blood damage indices from *in-silico* cannula insertion configurations. The focus of the *in-silico* cannulation simulations presented in this study is to establish the consequence cannula orientation on the sub-lethal hemolysis. The methods summarized above are presented with more detail in the following sections:

2.1. Micro CT geometry reconstruction and model preparation

3D cannula reconstructions were obtained starting with scans from a SkyScan 1172 (Kontich, Belgium) X-ray computed tomography (micro-CT) system, with image resolution of 13.49 micrometers. Cannulae were scanned from the outflow tip and included 5 cm of the cannula body. On average, 273 projections were obtained from each scan, which were reconstructed using in-house filtered backprojection MATLAB (The Mathworks Inc, Natick, MA) codes in order to recover slice data along the longitudinal axis of the cannula. Reconstructed 2D slice data were further processed in ScanIP (Simpleware, Exeter, UK) for slice-wise segmentation of the cannula geometry, using a thresholding algorithm. Smooth 3D inner and outer triangulated surface reconstructions of the scanned cannulae were created by first applying a Gaussian smoothing filter to each segmented slice image and subsequently introducing the resulting surfaces into Geomagic Studio 10 (Durham, NC) for minor surface repairs and smoothing before finally converting into a NURBS surface for exporting as an IGS model. The IGS model was finally imported into Pro/Engineer where the model cannula was attached externally to the center of the square face of a cuboidal computational domain with dimensions of breadth equal to 10 cannula diameters (inlet to the domain). This procedure is illustrated in Fig. 2.

The choice of a cuboidal domain for jet flow confinement was designed for easy PIV access and also to be compatible with previous experimental and 2D numerical studies by Ouwa et al. (1986a, 1986b) on symmetric, asymmetric and wall jets in a rectangular domain. The computational domain length was considered as 100 inlet diameters based on numerical considerations for stability of the transient CFD pressure field solution, as well as suitability for accommodating the full length of developed jet streams at a flow rate of 0.3 L/min (Re ∼650 for blood) through the 8FR circular orifices.

Cannulae were attached externally to the cuboidal computational domain or inserted into it as per requirements to accommodate angular cut cannula tips. This same methodology was followed to insert a three-dimensional parametrically oriented end-hole 8FR cannula into a patient specific neonatal aorta model (Pekkan et al., 2008). The parameters chosen for cannula insertion included cannula insertion angle, insertion depth and outflow Re, in order to entertain a full gamut of clinically relevant CPB related scenarios. 3D surgeon sketches describing pediatric CPB cannulation were used as a reference in order to orient the cannula and aortic arch with respect to each other in a typical standard CPB outflow configuration, directing flow along the transverse arch towards the descending aorta. A second more arbitrary orientation of aortic cannulation—directing flow toward the walls of the transverse arch, was also prepared in order to study the effect of cannula orientation on hemolysis.

2.2. Computational model and solver

The CFD flow domains were discretized into unstructured Cartesian immersed boundary grids (Fig. 2). Direct numerical simulation was performed to solve the Navier–Stokes equations using a second-order accurate, finite difference method; in-house cardiovascular flow solver has been used extensively for image-based hemodynamic modeling and incorporates a validated multi-grid artificial compressibility numerical solver (Le et al., 2010; Payli et al., 2007;
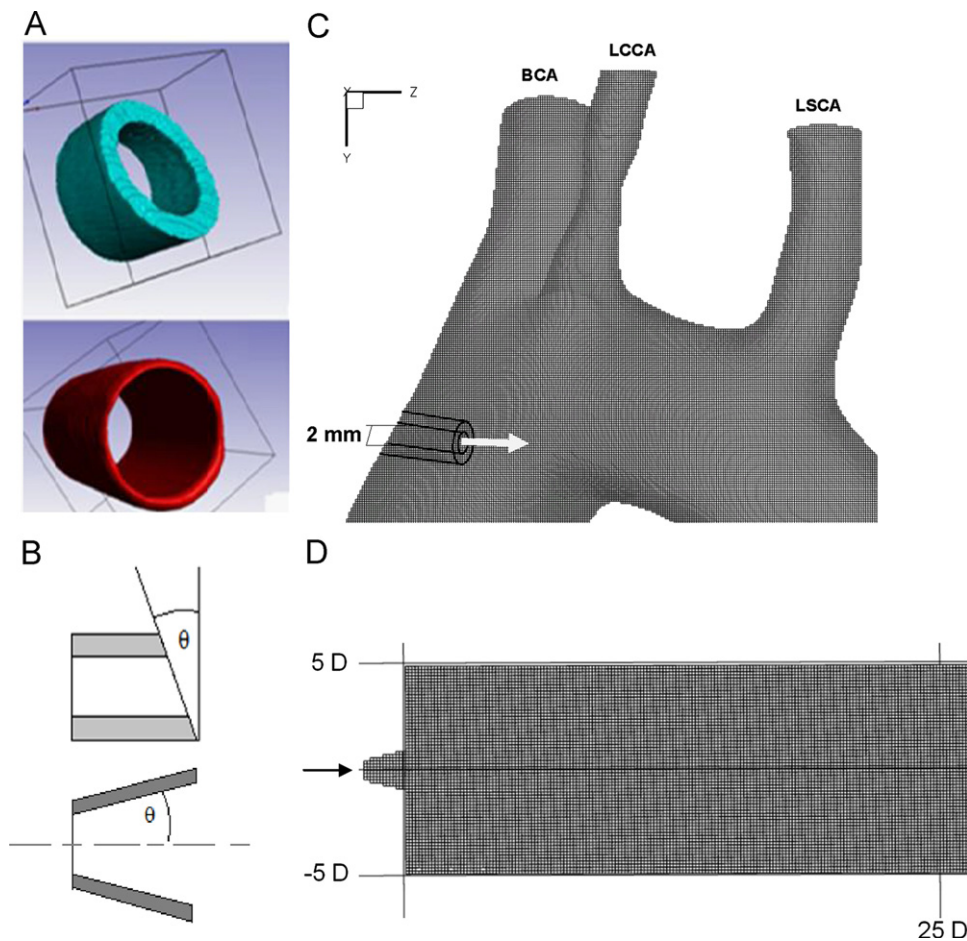
Fig. 2. (A) Three-dimensional micro-CT reconstructions of two pediatric cannula tip geometries analyzed in this study: DLP Medtronic 77008 (top) and RMI FEM II-008-ATI (bottom). (B) Parametric illustrations of oblique cut cannula tip design and a diffuser cone tip design. (C) and (D) Example unstructured Cartesian immersed boundary grids for a neonatal aortic arch model with and inserted end-hole cannula indicated by a wireframe (top), and a cuboidal test-rig domain with a 15° diffuser cannula (bottom) measured in terms of inlet diameter, D (2 mm), respectively. The cuboidal computational domain was $10 \times 10 \times 100$ D in size.

Pekkan et al., 2009). Incompressible and Newtonian blood flow with constant hemodynamic properties ($\rho = 1060$ kg/m^3, $\mu = 3.71 \times 10^{-3}$ Pa s) was employed and no-slip boundary conditions were enforced at vessel and confining walls, which were assumed rigid and impermeable. The rigid wall assumption is a feasible one for continuous flow CPB situations such as those simulated in this study. The fluctuating components of velocity i.e., u', v', w', and turbulent kinetic energy (TKE) for the end-hole cannula jet at Re 2150 was quantified using the instantaneous flow field velocity along with the running average velocity at steady inflow. The averaged integrated value of TKE in the jet-wake fluctuated about a constant value converging to within 10^{-2} m^2/s^2 as the grid resolution was improved; indicating consistency and grid independence of the numerical solution. Grid resolution was qualified using the viscous length scale, y^+, which was chosen to be of the order of unity for sufficient DNS resolution (Valen-Sendstad et al., 2011). Similarly, t^+, the time scale, was also chosen as unity in reference to the grid spacing and maximum simulated flow Re, after inlet normalization of length and velocity. Δt for the simulation was considered as 0.01 dimensionless simulation time units; one time unit was of the order O(10^{-5}) s. To describe this spatio-temporal resolution strategy in context, an Re 2150 jet (the highest speed jet modeled in our study) delivering 0.71 L/min of blood from 8FR (2 mm) internal orifice supplies energy at the rate ~ 7.5 W/kg or 7.5 m^2/s^2; therefore making the Kolmogorov length-scale, $\eta = (\nu^3/\varepsilon)^{1/4} = 4.89 \times 10^{-5}$ m. In contrast, the corresponding Taylor micro-scale is 4.03×10^{-4} m, which is the required minimum resolution to observe turbulent wake structures in the jet. Since our cuboidal test-rig simulations were all resolved at $\sim 3 \times 10^{-4}$ m, which led to ~ 7.5 M nodes in the cuboidal test rig domain i.e., was $\sim 8 \times$ larger than the Kolmogorov scale resolution. However, at this resolution the Taylor microscale was sufficiently resolved. The spatial grid resolution for the *in-silico* aortic arch simulations was finer than the cuboidal test rig domain simulations and also had ~ 7.5 M nodes in the aortic arch, in order to have improved resolution in the more complex geometry. As such, a turbulence model was not employed, but the stringent criteria for spatio-temporal resolutions ensured good resolution of downstream jet hemodynamics.

CFD simulations were conducted at Pittsburgh Supercomputing Center's Blacklight and Pople supercomputing cyber-infrastructures using a stable and parallel scalable high-performance computing (HPC) version of the in-house CFD solver code. Each simulation was terminated after 18,500 simulation time steps (~ 0.37 s at Re 1000) and cost an average of 2000 service units each i.e., equivalent to 250 h at 8 core parallelism. Convergence of the transient CFD solution was monitored using the time-evolution of the running average jet axial velocity at several axial locations of the jet, for up to 10 inlet diameters.

2.3. Blood damage, thrombosis and flow structures

Device-related thrombosis in the jet wake is hypothesized to be a major factor in medical device design. Further, insertion of cannulae into the aorta can lead to non-physiological load and stress on blood cells and the vascular walls due to the high velocity and exit force which is different for any given surgical orientation of the cannula jet. Predictions of blood damage may be made from CFD either using Lagrangian particle tracking (Alemu and Bluestein, 2007; Apel et al., 2001; Grigioni et al., 2004; Nobili et al., 2008; Yin et al., 2004) or convection Eulerian (Farinas et al., 2006; Garon and Farinas, 2004) damage functions based on empirical power laws, time history of stress exposure, viscous energy dissipation, and transient turbulence. In this study, normalized index of hemolysis (NIH) was computed by a stress-based Lagrangian approach, proposed by Giersiepen et al. (1990) using pathlines from each simulated jet stream. Physically, NIH may be regarded as equivalent the hemoglobin released per pass of blood volume through a given volume region of interest in the flow field and an NIH under 0.01 g/100 L is regarded as a design goal for mechanical circulatory support blood pumps. For consistency, an identical number of particles (788 massless particles) were released from identical start positions at the inlet of the cannulae, using Tecplot (Bellevue, WA) macros, and shear accumulation was computed along the pathlines. Damage index. D, was accumulated using the modified time integration step employed by Mitoh et al. (2003).
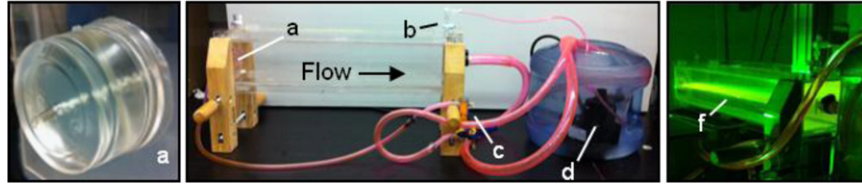
Fig. 3. Illustration of the in-vitro flow loop with a $10 \times 10 \times 50$ cm^3 cuboidal jet-flow test rig for high-speed image capture and PIV of jet wake. (a) Cannula in PDMS insert plug; (b) air release valve for priming; (c) rotometer; (d) pump and reservoir; (f) Snapshot of 2–3 mm thick PIV laser sheet through a longitudinal slice of the jet.

In this manuscript, results are presented relative to the Re 650 jet NIH hemolysis index, for effective relative comparison. The rationale for reference normalized NIH representation has been presented in the Appendix as a means to discount for the effects of variability in reported hemolysis results using different shear-based power-law blood-damage models, such as those proposed by Song et al. (2004). A scalar stress value, SS_{mag}, was computed from the shear stress tensor, τ, using the Von-Mises criterion which is calculated from the six components of the stress tensor: as follows:

$$SS_{mag} = \left[\frac{1}{3}\left(\tau_{ii}^2 + \tau_{jj}^2 + \tau_{kk}^2\right) - \frac{1}{3}\left(\tau_{ii}\tau_{jj} + \tau_{jj}\tau_{kk} + \tau_{kk}\tau_{ii}\right) + \left(\tau_{ij}^2 + \tau_{jk}^2 + \tau_{ki}^2\right) \right]^{1/2} \quad (1)$$

NIH was computed using normal estimates for hematocrit and hemoglobin content of 45% and 150 g/L, respectively.

Spatial energy dissipation provides a qualitative map of the hemolysis in a jet stream (Bluestein and Mockros, 1969) and showed resemblance to the shear stress fields in each of the simulated flow fields. This is computed using the following formulation:

$$E_{diss} = 2\mu \left(\left(\frac{\partial u}{\partial x}\right)^2 + \left(\frac{\partial v}{\partial y}\right)^2 + \left(\frac{\partial w}{\partial z}\right)^2 \right) + \mu \left(\left(\frac{\partial v}{\partial x} + \frac{\partial u}{\partial y}\right)^2 + \left(\frac{\partial w}{\partial y} + \frac{\partial v}{\partial z}\right)^2 + \left(\frac{\partial u}{\partial z} + \frac{\partial w}{\partial x}\right)^2 \right) \quad (2)$$

Here, u, v, w are the components of the velocity vector, and E_{diss} at each CFD grid location is reported in this manuscript as a normalized ratio to the peak dissipation in the Re 650 end-hole jet, for qualitative comparison of the different simulated jet cases. Ensemble integrated E_{diss} was computed in order to obtain a single scalar value representative of the energy dissipation in each simulated jet wake.

Vortical structures seen in two in-silico aortic cannulation configurations were qualified using the Q-criterion formulated by Hunt et al. (1988) which is defined by the difference between the squares of the Euclidian norms of vorticity, Ω, and strain rate, S, such that: Q-criterion $= 1/2(|\Omega|^2 - |S|^2) = 1/2\ L_{ij}L_{ij}$, in Einstein's summation convention, where L_{ij} is the velocity gradient tensor.

2.4. Empirical models for jet characterization

CFD results were fitted to analytical models for a circular orifice jet axial velocity profile presented in Gauntner et al. (1970) (Gauntner et al.). This approach provides a validation case of the present CFD results and insight into the axial profiles of jet outflow velocity for laminar and turbulent neonatal cannula flow regimes. The model is fitted against CFD velocity data after the region of flow establishment characterized by the jet's potential core length. Mathematically, the potential core length for a 3D parabolic inlet velocity profile in a circular orifice is defined by the axial distance up until which the maximum jet velocity equals the mean orifice outflow velocity i.e., $|V| = |V_{inlet}|_{max}/2$ for a parabolic inlet profile at a circular orifice. The axial component of jet velocity in the region of established flow was fitted to the following mathematical model:

$$\frac{U_{max,\ axial}}{U_{mean,inlet}} = a(Re)^b \left(\frac{X}{D}\right)^c \quad (3)$$

where: a, b and c are constants. MATLAB curve fitting toolbox was employed to obtain parameters a and b, by constraining an inverse relationship between Re and X/D i.e., setting $c = b^{-1}$. End-hole cannula jet CFD data were fit to this model until an axial distance of 100 inlet diameters for Re 650, 850 and 2150 jet streams, after ~ 0.3 s from initiation of each jet.

2.5. Flow boundary conditions

Cuboidal test-rig jet flow characterization studies and in-silico aortic cannulation flow simulations were conducted using parabolic inlet velocity profiles at circular cannula inlets. Jet flow characterization studies were conducted for steady inlet flow conditions ranging between Re 650 and Re 2150 i.e., 0.3 to 1.0 L/min. Flow simulations in the aortic arch model were performed assuming a steady blood flow rate corresponding to Re 2150, assuming 100% cannulation from an 8FR end-hole cannula, with a cross-clamped ascending aorta. A mass flow preserving outflow boundary condition was applied at outlet of the cuboidal test

rig as well as at the aortic outflow branches, considering a 40–60% flow split between head-neck vessels and the descending aorta (Fogel et al., 1999; Pekkan et al., 2008). Flow-split weighting coefficients of head-neck vessels were calculated proportional to the area of each artery as 0.2, 0.08, and 0.12 for the innominate, left common carotid, and left subclavian arteries.

### 2.6. Experimental flow visualization and PIV

Time-resolved dye flow visualization of the starting jet wake was performed in an experimental version of the cuboidal test-rig constructed from 0.220″ Lexicon plexiglass. The internal surface of the flow chamber encloses a rectangular prism of $10 \times 10 \times 50$ cm. Each device-specific cannula tip was centrally inserted 5 mm into the flow chamber using a tapered Polydimethylsiloxane (PDMS) plug that was pressure-fit into a central hole in the inlet face of the rig. This inlet configuration allows multiple cannulae tips to be interchangeably fit into the same rig. The flow loop was powered by a submersible pump in an 11 L reservoir, controlled by a variable transformer to obtain desired physiological flow rates, using water as working fluid. A comprehensive illustration of the in-vitro loop setup is shown in Fig. 3. 1024×1024 pixel 12-bit mono color image acquisitions were accomplished at 250 FPS using a high-speed CMOS camera (Photron FASTCAM SA4). Flow fields were compared qualitatively with downstream jet wake hemodynamics obtained from our CFD studies in a similar cuboidal domain.

In addition, a second in-vitro flow setup was employed to characterize jet axial pressure–flow characteristics. Jet axial pressure measurements were obtained 70 mm downstream of the cannula inlet and immediately downstream of the submersible pump, using TruWave disposable pressure transducers (Edwards Life Sciences, Irvine, CA, USA). In order to identify the contributions of the diffuser to improved jet dynamics, pressure measurements were made at Re 2150 flow along the jet axis for a rapid-prototyped model of a cannula tip with a 15° diffuser cone tip, having cone inlet diameter of 2 mm. Pressure–flow characteristics were compared against those obtained for the 8FR RMI end-hole cannula tip, at identical flow conditions.

Finally, 2D time-resolved PIV studies were also conducted using the cuboidal test rig with $5.0 \times$ scaled up (~ 10 mm inner diameter) rapid-prototype replicas of the device-specific cannulae in order to quantify experimentally observed jet wake velocity fields and also to provide a means for validation of CFD results at Re 650, for the RMI and DLP cannulae. Scaled up models were employed in order to have a better representation of velocity fields in the jet, due to limitations in reducing laser sheet thickness to under 2 mm, The working fluid for PIV was water seeded with 0.1 g/L of 10–12 micron diameter hollow glass microspheres (density ~ 1.1 g/cc) by TSI, Inc.. A standard PIV system was used to acquire 2D velocity field measurements with a laser sheet thickness of approximately 2.5 mm. The system consisted of one Nd:YAG lasers (Model Twins BSL 50, Quantel) with an energy of 50 mJ per pulse at 532 nm and operated at a repetition rate of 15 Hz. The image pairs were recorded using a CCD camera (Model Imager Pro X 2M, LaVision, Germany) and a series of 83 image pairs were acquired to obtain the field of view 39×29 mm^2 at spatial resolution of 24 μm/pixel. Two adjacent frame acquisitions were made along the axis of each device-specific jet studied using PIV, in order to obtain a larger field of view. A laser pulse delay time of 2000 μs was used to maximize particle image displacement without loss of correlation for an initial interrogation window size of 32×32 pixels and a final interrogation window size of 16×16 pixels. Interrogation windows were overlapped by 50% to satisfy the Nyquist sampling criterion. Peak velocity observed in the developing jet was recorded for preliminary comparison against CFD results.

3. Results

CFD simulations examining jet streams for viscous energy dissipation have focused novel cannula tip design efforts towards a diffuser tip design. Simulations performed for varying diffuser cone angle and flow conditions have led to the development of a novel 15° diffuser tip design for optimal hemodynamic performance and minimal blood damage that has shown a 50%
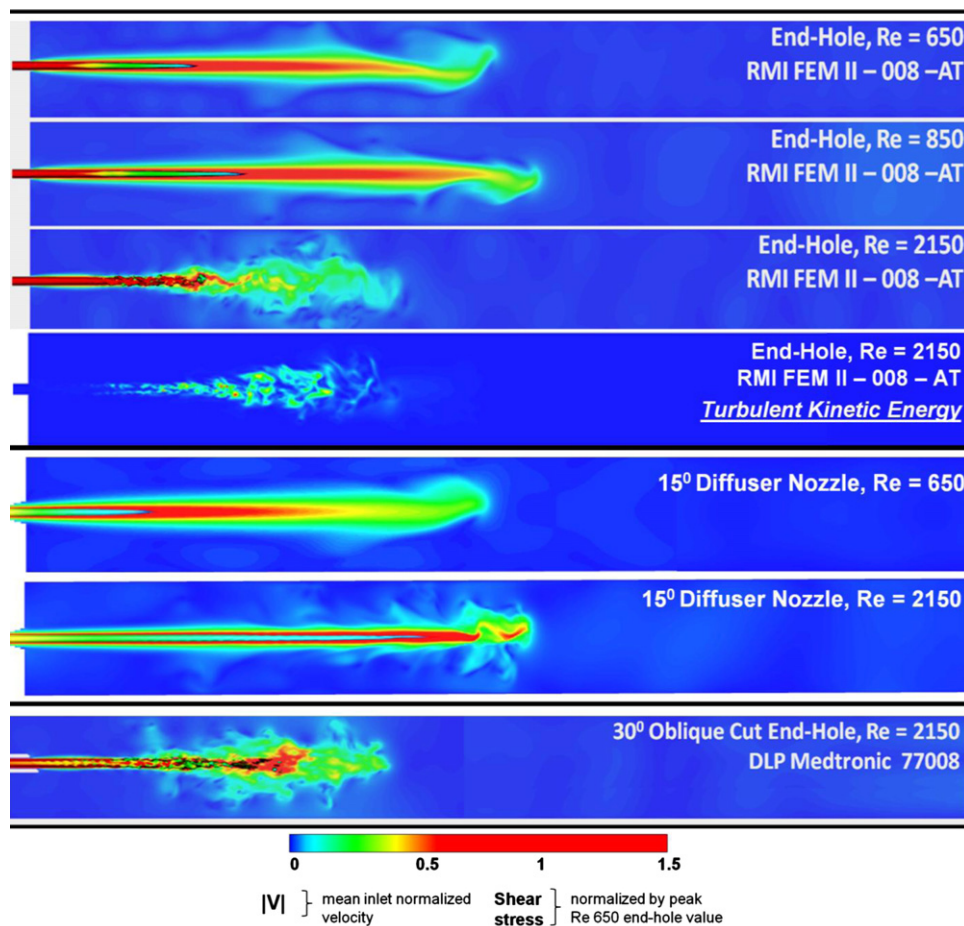
Fig. 4. Inlet-normalized velocity field comparison between an RMI end-hole cannula tip, a 15° diffuser tip and the DLP oblique-cut tip jets, for Re 2150 ($\sim$1 L/min blood flow rate), $\sim$0.3 s from the start of jet flow. Also shown is a comparison of developing jet lengths, visualized using velocity magnitude iso-surfaces for $|V| = |V_{\text{inlet}}|_{\text{max}}/2$, colored by Re 650 end-hole peak normalized shear stress magnitude. Potential core length increases with increasing Re within the laminar flow regime. The developing jet region of flow establishment was not clearly demarcated in case of turbulent jet streams. The quickly progressing Re 2150 15° diffuser tip jet with a clearly defined developing length draws distinction against the turbulent Re 2150 oblique-cut and end-hole jets which dissipates far more energy along its potential core, therefore leading to a shorter overall jet axial length. Turbulent kinetic energy (TKE) – plotted only for Re 2150 end-hole jet – was primarily observed in the jet wake.

improvement in viscous energy dissipation when compared with the conventional end-hole cannula jet at flow rates of $\sim$1 L/min.

3.1. Cuboidal test-rig simulations

CFD simulated jet regimes were congruent with the jet regime classification provided in Gauntner et al. (1970) and Re 650 jets were observed to demonstrate laminar physics in comparison with the higher speed Re 2150 jet. High frequency oscillations in TKE (domain integrated average) observed at Re 2150 were characteristic of free-jet turbulence and as illustrated in the velocity magnitude snapshots through a longitudinal slice of the Re 2150 end-hole cannula tip, complex vortical structures and turbulent characteristics were observed in the jet wake $\sim$0.3 s from the start of flow. In comparison, the novel 15° diffuser tip design demonstrated a comparatively less complex jet wake at Re 2150 which dissipated less energy along its potential core length. Fig. 4 depicts the salient jet regions (developing potential core length and developed jet wake) for different cannulae in the cuboidal chamber and Fig. 5 compares these jets for spatial energy dissipation. The diffuser tip jet was noted to have higher spatial energy dissipation close to the cannula tip and lower values throughout the flow field in comparison with the standard end-hole jet streams at low and high physiological Re.

Potential core length highlighted by the mean-inlet velocity contour definition did not show a clear axial separation between the developing jet region and jet wake for the turbulent Re 2150 end-hole jets, which exhibited slower axial propagation rates and high dissipation across the early developing jet lengths. The 15° diffuser jet on the other hand had a shorter potential core length for Re 650 and a longer but clearly defined core for Re 2150 illustrating the efficacy of the diffuser design in delaying onset of shedding vortical wake structures. The highest energy dissipation for all cannula jets was observed within the region of flow establishment (i.e., potential core region). The cannula jets exhibited strong vortex structures only after the axial distance for flow establishment (see Fig. 6) but the oblique cut end-hole cannula tips exhibited more complex asymmetric vortex shedding patterns in the jet wake in comparison with the end-hole or diffuser tip. Observed magnitude of spatial shear stress over the developing potential core jet length was found to decrease with the increase in oblique cut of the end-hole cannula tip. However, the ensemble total energy dissipation as well as hemolysis index was found to be higher for oblique cut end-hole cannula tip geometries due to more complex vortical structures in the jet wake. A summary of cumulative energy dissipation observed in the computational domain observed $\sim$0.3 s from jet
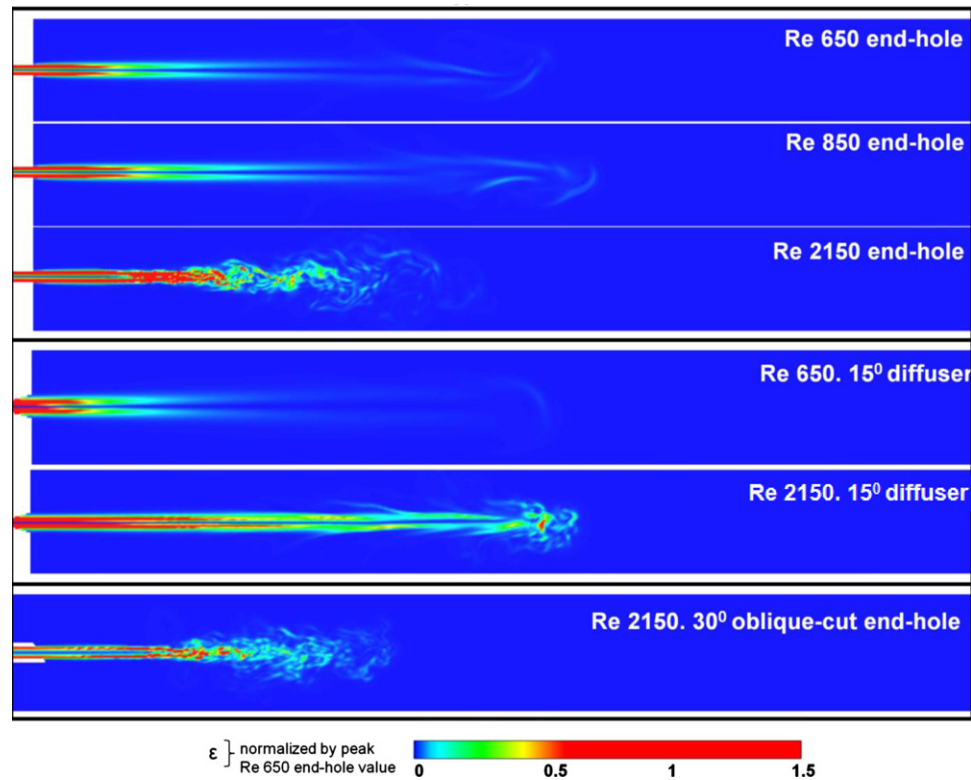
Fig. 5. Spatial energy dissipation (normalized by peak Re 650 energy dissipation) visualized in longitudinal slices though jet axis, acquired ~0.3 s from initiation of jet flow. Maximum energy dissipation was apparent in the developing jet region i.e., within the potential core length.
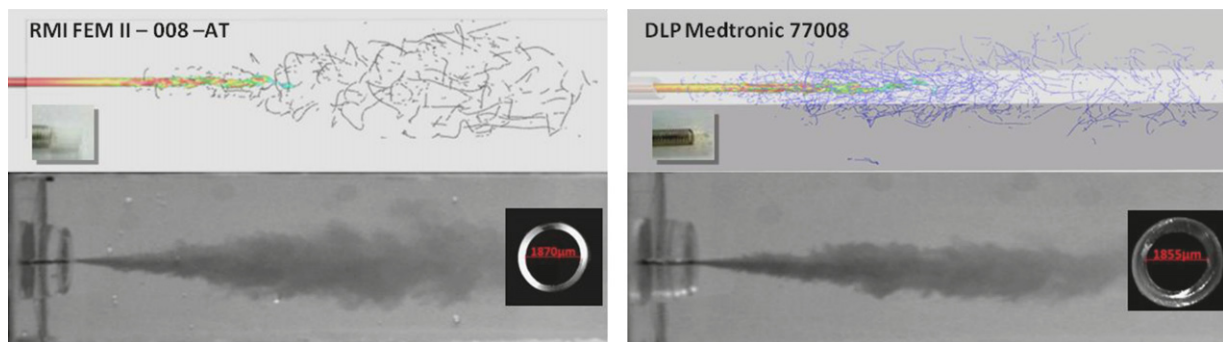
Fig. 6. Vortical structures are visualized using vortex cores computed in Tecplot for Re 2150 cannula jet streams 0.03 s from jet initiation for: (a) end-hole RMI cannula; (b) oblique cut end-hole DLP cannula. Each is compared with instantaneous snapshots from dye flow visualizations (below). There is visual concordance between the jet wake regions from CFD and experiment with regard to the axial location of dominant vortical structures downstream of the developing potential core length. Vortical structures are apparent within a shorter axial distance of the jet inlet for the DLP than the RMI tip. Potential core length is visualized using $|V| = |V_{inlet}|_{max}/2$, iso-surfaces colored by shear stress, normalized by peak Re 650 shear stress magnitude. Each device-specific cannula tip's internal surfaces revealed oval rather than perfectly circular internal surfaces.

flow initiation is summarized in Table 1, normalized with reference to the Re 650 end-hole jet.

Table 2 presents a summary of NIH for end-hole and 15° diffuser jets, at Re 650, 850 and 2150. Linear correlation was observed between the integrated E_{diss} values (Table 1) for each jet stream and the corresponding hemolysis indices (Table 2) computed for corresponding jets simulated in the cuboidal test-rig. The diffuser was found to outperform the end-hole jet with regards to both E_{diss} and NIH. An analysis of smoothed probability distributions (not shown) constructed for the shear damage, D, accumulated for different streamlines indicated that that Re 2150 end-hole jet damage accumulation was distributed over a wider range of higher D values than the slower Re 650 jet, supporting the correlation between sub-lethal hemolysis and Reynolds number, reported in Table 2.

3.2. Experimental flow visualization and jet characterization

Time-resolved dye flow visualizations were qualitatively found to resemble CFD simulated jet behavior (see Fig. 6). Dye flow visualizations represent both convection and diffusion transport of dye in the flow field and therefore provide only qualitative evidence of jet axial propagation i.e., axial distance of jet wake and local jet diameter; whereas, in contrast, PIV and CFD determine velocity fields that are instantaneous representations of the flow physics. PIV provided quantitative validation of numerical results in the developing jet region (near inlet). The CFD derived peak velocity in the developing Re 650 jet region (equivalent to 5.0–6.5 cm/s for water) as well as the range for slower moving complex shedding vortex structures (< 2 cm/s for water) at the shear layer of the jet were found to match well with observations

from PIV (Fig. 7). PIV also complemented the CFD observations from the vortex-core plots in Fig. 6 that indicate vortical structures are apparent within a shorter axial distance of the jet for the DLP oblique cut tip in comparison with the RMI end-hole tip.

Experimental pressure–flow analysis revealed that the static pressures drop 70 mm axially downstream from diffuser cone jet inlet was distinctly reduced for the same cannulation flow rate in comparison with the identically sized RMI end-hole cannula tip. Lower pressure gradients for the same flow rate are concordant with a weaker outflow jet i.e., lower exit force and outflow velocity,

Table 1
Summary of cumulative energy dissipation calculated for the instantaneous flow fields noted for different jet streams at ~0.3 s from start of jet flow, reported as a normalized ratio to the Re 650 end-hole result. Corresponding potential core length information is reported as a multiple of cannula inlet diameter, D. n the case of Re 2150 jets, a clear potential core defined by the axial extent of the $|V| = |V_{mean}|_{inlet}/2$ isocontour is not observed.

| Tip design	Re	Integrated net energy dissipation, ε	Potential core length (in inlet diameters, D)
End-hole (RMI)	650	1	20
	850	1.23	25
	2150	2.32	–*
15° diffuser	650	0.44	15
	2150	1.31	40
15° oblique cut	650	7.00	25
30° oblique cut (DLP)	650	10.17	30
	2150	15.80	–*

* Potential core length not distinctly demarcated using the isocontour definition.

Table 2
Summary of hemolysis index computations for end-hole and 15° degree diffuser jets, reported as a normalized ratio Re 650 end-hole result.

| Re	End-hole	15° diffuser
650	1.00	0.31
850	1.62	0.83
2150	4.10	3.45

supporting that the diffuser tip is more ideal than the end-hole tip with regard to producing a potentially less-damaging outflow jet in a cannulated aorta. Fig. 8 shows the pressure drop versus flow rate relationship for an end-hole and a diffuser tip jet, along the jet axis, in terms of equivalent flow-rates of blood after dynamical scaling. This plot indicates that the standard end-hole jet required a significantly higher driving pressure from the pump in order to propel axially forward, in comparison with the diffuser cone cannula tip, at the same flow rates. Therefore, the diffuser not only provides desirable jet flow characteristics by virtue of its potential core length, velocity field and blood damage (discussed in previous CFD analysis sections) but simultaneously has desirable pressure–flow characteristics which could potentially reduce the requirement of pumping pressures during CPB procedures. This characteristic of the diffuser tip requires further investigation in a more realistic experimental extra-corporeal circulation setting because apart from
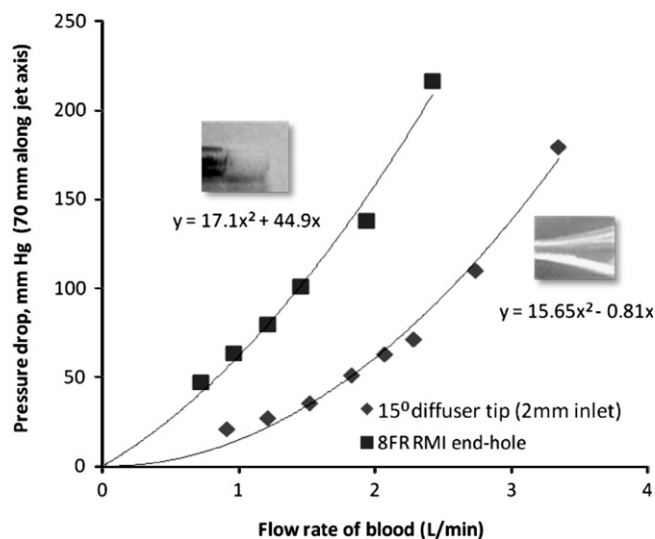
Fig. 8. Experimental characterization of pressure drop versus flow rate relationship for the jet along the jet axis, comparing a standard RMI 8FR end-hole cannula against 15° diffuser cone outflow tip.
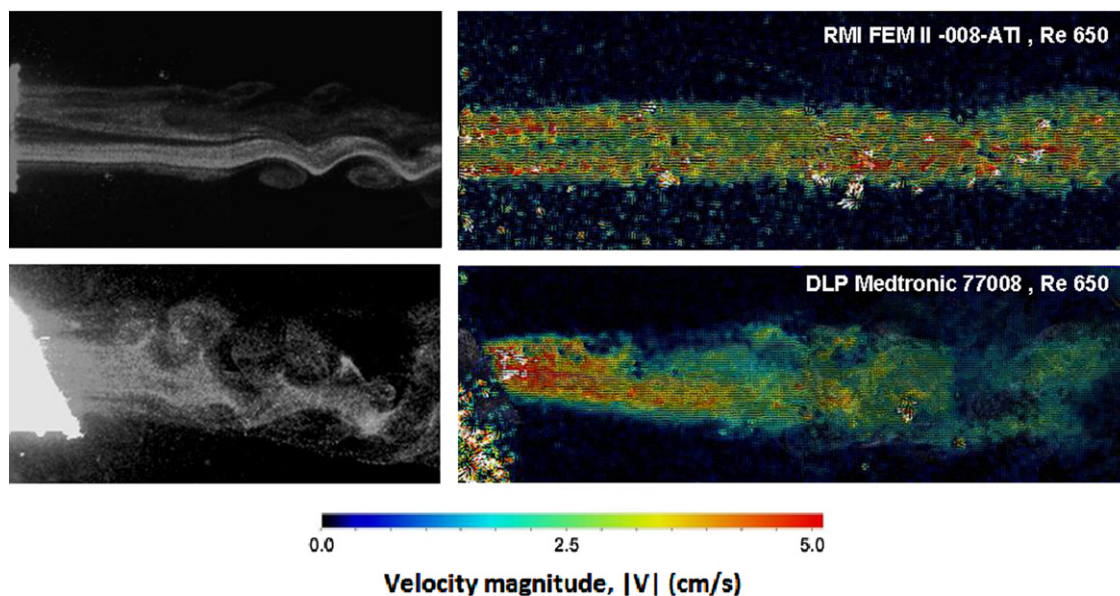
Fig. 7. Left: representative zoomed in particle injection instantaneous snapshots at Re 650, for a 5.0 × scaled up end-hole RMI laminar jet (top) and a more disturbed and unsymmetrical oblique cut DLP cannula jet, close to the inlet for 4 inlet diameters. Beautiful periodically shedding vortices are seen in the end-hole cannula jet shear layer, at low Re. Right: PIV flow fields for water jets through the RMI and DLP cannula tips, presented at Re 650.
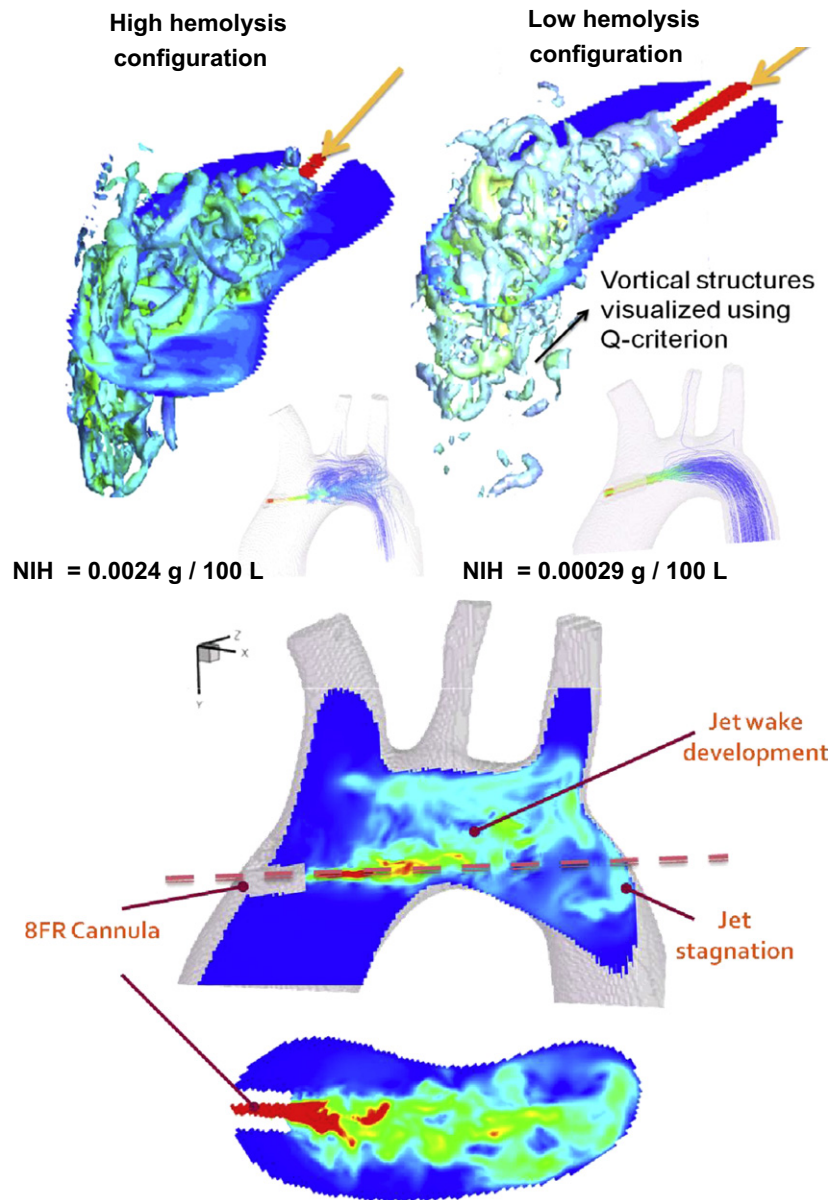
Fig. 9. Comparison between vortical structures created by an Re 2150 end-hole cannula jet stream in an *in-silico* cannulation setting, for two different insertion orientations, using iso-surfaces of Q-criterion > 0,overlaid on a slice through the center of the jet stream colored by the max-normalized resultant velocity field. Pathlines in flow field are shown colored by normalized shear stress magnitude. Velocity fields seen in cross sectional slice view-planes through a neonatal aorta model cannulated with an 8FR end-hole cannula are shown (bottom) for comparison with the jet wakes in the cuboidal chamber. Important regions of the cannula jet have been labeled. Effects of vascular geometry and in-vivo cannula orientation cannot be discounted.

the cannula tip design, the inner diameters of the cannula tip, cannulation angle relative to the aortic arch, as well as subject-specific aortic arch geometry will have significant roles to play in determining the pumping pressures.

3.3. Patient-specific in-silico cannula orientation simulations

Fig. 9 describes vortical structures seen in two *in-silico* aortic cannulation configurations qualified using the Q-criterion. Iso-surfaces of Q-criterion > 0 i.e., where the Euclidean norm of the vorticity tensor dominates that of the rate of strain, were utilized in order to visualize coherent vortex structures in the jet wake. The arbitrarily oriented cannulation case resulted in being a high hemoylsis configuration and complex vortex structures were apparent at the location of jet impingement upon the walls of the transverse aortic arch, which is undesirable due to close proximity to the head and neck vessels. In contrast, the

orientation prepared based upon the surgeon sketches resulted in a low hemolysis configuration where only a single coherent predominant vortex-core was observed around the irrotational jet core prior to jet impingement proximal to the descending aorta.

Table 3
Empirical model fit data for jet streams. Here, a, b, c are constants ($c=b^{-1}$) and D is the inlet diameter of the cannula.

$$\frac{U_{max,\,axial}}{U_{mean,inlet}} = a(\text{Re})^b \left(\frac{X}{D}\right)^c ; c=b^{-1}$$

Re	a	b	c
650 (end-hole)	0.83	0.94	−0.94
850 (end-hole)	0.84	0.76	−0.76
2150 (end-hole)	2.18	0.81	−0.81
650 (15° diffuser)	0.63	0.84	−0.84

These observations suggest the existence of optimal characteristics (outflow angle and insertion depth) for improved hemodynamic performance during surgery.

3.4. Empirical models for jet characteristics

In-silico cannula jet evaluations in the cuboidal test rig may be reduced to tractable empirical relationships for instantaneous axial jet velocity in the developed jet wake region, which may potentially be regarded as a simple rule of thumb for optimal jet stream based cannula tip choice in the operating room. The goal of empirical model fitting is also to allow case-specific CFD results to be generalized for a variety of fluid media, Reynolds numbers or cannula sizes, based on the theory of dynamic similarity. Table 3 indicates the parameters for empirical model fits for the axial component of velocity (normalized by mean inlet velocity) in the established jet region for three Re cases of the end-hole as well as the 15° diffuser tipped cannula. The fits indicate that the inverse relationship set by the proposed empirical model between Re and the axial distance from the orifice match the CFD data well. The turbulent Re 2150 end-hole jet was found to show augmented unsteady behavior after the potential core length than the Re 650 and Re 850 jets. However, despite these differences, the mean axial velocity after the region of establishment was found to fit well with the empirical model.

The length of the region of establishment (i.e., potential core) is an indication of resistance-to-outflow characteristic for a given cannula tip design. Visual inspection of energy dissipation along the axial length of the jet from Fig. 5 indicates that the highest energy dissipation occurred upstream of the potential core axial length. This is corroborated by the results in Table 1 which highlight a direct relationship between potential core length and energy dissipation for a given cannula tip. For the same flow Re, a shorter potential core is an indicator of less resistance to outflow and lesser energy dissipation in the developing jet region. The oblique-cut cannula tips were observed to demonstrate higher net energy dissipation ratings than end-hole whereas their potential core lengths were comparable to the end-hole jets, indicating that the increased energy dissipation in these jets was a consequence of shear–layer interactions in the jet wake. Increasingly angular oblique-cut tips were observed to have greater net energy dissipation and longer potential cores, for the same Re (Table 1).

In the case of axisymmetric jets, the characteristic velocity can be taken as the local centerline velocity of the jet, i.e., $U(x)$, which has an inverse relationship with axial length, x i.e., proportionality with $1/x$ (Dimotakis, 2000). An inverse relationship was observed between centerline velocity and axial distance based on robust empirical curve fits to our CFD results (Table 3), which conforms to expectations in the developed jet region. Since the local length scale for the round jet is typically taken as the local jet diameter, $L(x)$, which is proportionate to jet axial distance, the local Re of the jet is proportionate to $U(x) \times L(x)$, the local Re of the jet is a constant along the jet-axial direction. This provides a basis for numerical choices for grid resolution in jet flow studies based upon Re, since a single Re can be used as a metric to determine the length and time scales required to resolve the flow completely in the entire domain.

4. Discussion

Submerged jets are characterized by four distinct states as a function of the Re number: (a) dissipated-laminar; (b) laminar; (c) semi-turbulent; and (d) turbulent. Dissipated laminar jets are unstable because the inlet jet momentum is quickly dissipated to the surrounding fluid typically less than six diameters beyond the inlet (McNaughton and Sinclair, 1966), which was not seen for the minimum flow Re 650 jets. Jet penetration depth increases with larger values of Re but in downstream jet regions the azimuthal velocity component (V_Θ) oscillates with exponentially increasing amplitude over time due to Kelvin–Helmholtz instability before fully dissipating. These instabilities were observed in the Re 650 and Re 850 cannula jets. Numerical simulations for circular jets have shown that at the critical Re number of 225 different types of flow instabilities are exhibited (Danalia et al., 1997). Ouwa et al. (1986a, 1986b) reported from experiments using Doppler velocimetry and dye injections for streamlines in 2D rectangular channels that symmetric confined jets begin to show asymmetric flow patterns after a Re of 30. Since the range of Re seen in neonatal and pediatric CPB scenarios and those studied in our jet flow simulations are between ~20 and 100 times this range, the simulated asymmetric flow patterns soon after the inlet are justified. These patterns were also observed in out flow visualization experiments. Experiments on scalar-mixing behavior in non-reacting round jets have indicated that a qualitative transition to full turbulence and turbulent-mixing behavior for Re only in the vicinity of 10,000 (Dimotakis, 2000). Therefore, the highest speed (Re 2150) jet flows that we simulate in this study may still be regarded as transitional rather than fully-developed turbulence.

In free single jet flows, the primary sources of vorticity are the dissipating transient jet wake and the shear layers along the jet boundary layer surrounding the irrotational jet core. Confined jet flows in physiological settings demonstrate additional complexity due to wall influence. Therefore, although pressure across the cannula tip (gauged using line-pressure in the heart-lung machine) is the common means of determining the operating point and choice of cannula based on flow rate which is usually chosen in order to maintain the cardiac index of the patient to between 2 and 2.5, this study suggests that in order to choose a cannula based on desirable jet flow hemodynamics, the potential core length, resistance to outflow, and NIH for a cannula jet at a chosen operating flow rate are major parameters. In an 8FR neonatal cannula jet, the main source of hemolysis is the sub-lethal damage of the red blood cells due to leaking of hemoglobin rather than damage due to rupturing at extremely shear rates above 42,000 s^{-1} (Leverett et al., 1972). In-vitro hemolysis tests will be required to be carried out in future studies in order to validate NIH estimates from CFD data in this study.

The diffuser cannula tip demonstrated in this study has been shown to remain laminar at high Re flow, reduce outflow velocity, improve hemolysis performance and improve pressure–flow characteristics of the cannula jet. Despite the advantages of the diffuser design, issues of increased local energy dissipation and the Coanda effect documented in the aortic cannula design literature (Joubert-Hubner et al., 1999; Magilligan et al., 1972) which is the property of a jet stream to adhere to the boundary wall, both become pronounced at high diffuser angles. This in-turn may limit its desirable effects of the diffuser design.

Future studies will be required to examine the effect of flow pulsatility on hemolysis and energy dissipation in the jet wake. Aortic arch CFD models may be improved using more realistic representation of the downstream aortic vasculature incorporating impedance based analog models (Dur et al., 2011; Vignon-Clementel I et al., 2006) that can be tuned accurately to simulate flow oscillations. CFD analyses of jet wakes through optimal cannula positioning studies performed using a two-way coupling approach between a parametric model geometry and real-time CFD data can provide inverse optimization criteria for deriving optimal intra-operative cannula insertion and orientation guidance during time-critical CPB operations. This can potentially guide further cannula tip design improvements, internal flow control features

and patient-specific cannula insertion configurations for optimal perfusion and decreased risk of thrombo-embolism during extra-corporeal circulation.

5. Conclusion

CFD was employed to delineate baseline hemodynamic performance of jet wakes emanating from pediatric/neonatal cannula tips used in current clinical practice as well as some novel designs, using DNS CFD in a cuboidal test rig. A diffuser cannula tip has been shown to posses passive jet flow control, hemodynamic performance and reduce exit force. Several diffuser cone angles require to be analyzed to arrive at an optimal diffuser inlet. This study also suggests that optimal outflow angle and insertion depth of aortic cannulation may lead to upto a 10-fold improved NIH performance during surgery. Innovative introducers specially designed for tiny pediatric aortas will be required for efficient, adequate and safe connection of diffuser tipped aortic cannulae to the intracorporeal circulation. The jet flow design paradigm demonstrated in this study represents a philosophical shift for cannula design practice which simultaneously accounts for engineering favorable pressure-drop versus flow-rate characteristics.

Conflict of interest statement

This statement is to declare that we, the authors of the manuscript, do not possess any financial relationships that might bias our work. We hereby declare that no conflict of interest exists in our work.

Acknowledgements

Appendix A. Supplementary information

Supplementary data associated with this article can be found in the online version at http://dx.doi.org/10.1016/j.jbiomech.2012.10.029.

References

Alemu, Y., Bluestein, D., 2007. Flow-induced platelet activation and damage accumulation in a mechanical heart valve: numerical studies. Artificial Organs 31, 677–688.

Andropoulos, D.B., Brady, K.M., Easley, R.B., Fraser Jr., C.D., 2010. Neuroprotection in pediatric cardiac surgery: what is on the horizon? Progress in Pediatric Cardiology 29, 113–122.

Apel, J., Paul, R., Klaus, S., Siess, T., Reul, H., 2001. Assessment of hemolysis related quantities in a microaxial blood pump by computational fluid dynamics. Artificial Organs 25, 341–347.

Bluestein, M., Mockros, L.F., 1969. Hemolytic effects of energy dissipation in flowing blood. Medical and Biological Engineering 7, 1–16.

Danalia, I., Dusek, J., Anselmet, F., 1997. Coherent structures in a round, spatially evolving, unforced, homogeneous jet at low Reynolds numbers. Physics of Fluids 9, 3323–3342.

De Wachter, D., De Somer, F., Verdonck, P., 2002. Hemodynamic comparison of two different pediatric aortic cannulas. International Journal of Artificial Organs 25, 867–874.

Dimotakis, P.E., 2000. The mixing transition in turbulence. Journal of Fluid Mechanics 409, 69–98.

Dur, O., Coskun, S., Coskun, K., Frakes, D., Kara, L., Pekkan, K., 2011. Computer-aided patient-specific coronary artery graft design improvements using CFD coupled shape optimizer. Cardiovascular Engineering and Technology 2, 35–47.

Farinas, M.I., Garon, A., Lacasse, D., N'Dri, D., 2006. Asymptotically consistent numerical approximation of hemolysis. Journal of Biomechanical Engineering 128, 688–696.

Fogel, M.A., Weinberg, P.M., Rychik, J., Hubbard, A., Jacobs, M., Spray, T.L., Haselgrove, J., 1999. Caval contribution to flow in the branch pulmonary arteries of Fontan patients with a novel application of magnetic resonance presaturation pulse. Circulation 99, 1215–1221.

Garon, A., Farinas, M.I., 2004. Fast three-dimensional numerical hemolysis approximation. Artificial Organs 28, 1016–1025.

Gauntner, J.W., B, L.J.N., Hrycak, P., 1970. Survey of Literature on Flow Characteristics of a Single Turbulent Jet Impinging on a Flat Plate, NASA TN D-5652. Lewis Research Center, National Aeronautics and Space Administation, Cleveland, OH.

Giersiepen, M., Wurzinger, L.J., Opitz, R., Reul, H., 1990. Estimation of shear stress-related blood damage in heart valve prostheses—in vitro comparison of 25 aortic valves. International Journal of Artificial Organs 13, 300–306.

Grigioni, M., Daniele, C., Morbiducci, U., D'Avenio, G., Di Benedetto, G., Barbaro, V., 2004. The power-law mathematical model for blood damage prediction: analytical developments and physical inconsistencies. Artificial Organs 28, 467–475.

Grigioni, M., Daniele, C., Morbiducci, U., D'Avenio, G., Di Benedetto, G., Del Gaudio, C., Barbaro, V., 2002. Computational model of the fluid dynamics of a cannula inserted in a vessel: incidence of the presence of side holes in blood flow. Journal of Biomechanics 35, 1599–1612.

Hunt, J.C.R., Way, A., Moin, P., 1988. Eddies, Stream, and Convergence Zones in Turbulent Flows.

Joubert-Hubner, E., Gerdes, A., Klapproth, P., Esders, K., Prosch, J., Henke, P., Pfister, G., Sievers, H.H., 1999. An in-vitro evaluation of aortic arch vessel perfusion characteristics comparing single versus multiple stream aortic cannulae. European Journal Cardio-Thoracic Surgery 15, 359–364.

Kaufmann, T.A., Hormes, M., Laumen, M., Timms, D.L., Linde, T., Schmitz-Rode, T., Moritz, A., Dzemali, O., Steinseifer, U., 2009a. The impact of aortic/subclavian outflow cannulation for cardiopulmonary bypass and cardiac support: a computational fluid dynamics study. Artificial Organs 33, 727–732.

Kaufmann, T.A., Hormes, M., Laumen, M., Timms, D.L., Schmitz-Rode, T., Moritz, A., Dzemali, O., Steinseifer, U., 2009b. Flow distribution during cardiopulmonary bypass in dependency on the outflow cannula positioning. Artificial Organs 33, 988–992.

Le, T.B., Borazjani, I., Sotiropoulos, F., 2010. Pulsatile flow effects on the hemodynamics of intracranial aneurysms. Journal of Biomechanical Engineering 132, 111009.

Leverett, L.B., Hellums, J.D., Alfrey, C.P., Lynch, E.C., 1972. Red blood cell damage by shear stress. Biophysical Journal 12, 257–273.

Magilligan Jr., D.J., Eastland, M.W., Lell, W.A., DeWeese, J.A., Mahoney, E.B., 1972. Decreased carotid flow with ascending aortic cannulation. Circulation 45, I130–133.

McElhinney, D.B., Tworetzky, W., Lock, J.E., 2010. Current status of fetal cardiac intervention. Circulation 121, 1256–1263.

McNaughton, K., Sinclair, G., 1966. Submerged jets in short cylindrical flow vessels. Journal of Fluid Mechanics 25, 367–375.

Mitoh, A., Yano, T., Sekine, K., Mitamura, Y., Okamoto, E., Kim, D.W., Yozu, R., Kawada, S., 2003. Computational fluid dynamics analysis of an intra-cardiac axial flow pump. Artificial Organs 27, 34–40.

Montoya, J.P., Merz, S.I., Bartlett, R.H., 1991. A standardized system for describing flow/pressure relationships in vascular access devices. ASAIO Transactions 37, 4–8.

Nobili, M., Sheriff, J., Morbiducci, U., Redaelli, A., Bluestein, D., 2008. Platelet activation due to hemodynamic shear stresses: damage accumulation model and comparison to in vitro measurements. ASAIO Journal 54, 64–72.

Osorio, A.F., Osorio, R., Ceballos, A., Tran, R., Clark, W., Divo, E.A., Argueta-Morales, I.R., Kassab, A.J., Decampli, W.M., 2011. Computational fluid dynamics analysis of surgical adjustment of left ventricular assist device implantation to minimise stroke risk. Computer Methods in Biomechanics and Biomedical Engineering 21, 21.

Ouwa, Y., Watanabe, M., Matsuoka, Y., 1986a. Behavior of a confined plane jet in a rectangular channel at low Reynolds number I. General flow characteristics. Japanese Journal of Applied Physics 25, 754–761.

Ouwa, Y., Watanabe, M., Matsuoka, Y., 1986b. Behavior of a plane jet at low Reynolds Number confined in a rectangular channel II. Two solutions by numerical analysis. Japanese Journal of Applied Physics 25, 1736–1740.

Payli, R., Pekkan, K., Zelicourt, D., Frakes, D., Sotiropoulos, F., Yoganathan, A., 2007. High performance clinical computing on the TeraGrid: patient-specific hemodynamic analysis and surgical planning, TeraGrid 2007 Conference Madison, WI.

Pekkan, K., Dur, O., Sundareswaran, K., Kanter, K., Fogel, M., Yoganathan, A., Undar, A., 2008. Neonatal aortic arch hemodynamics and perfusion during cardio-pulmonary bypass. Journal of Biomechanical Engineering 130, 061012.

Pekkan, K., Dur, O., Zelicourt, D., Payli, R., Sotiropoulos, F., Kowalski, W., Chen, C., Patrick, M., Kara, L., Keller, B., 2009. Embryonic Intra-Cardiac Flow Fields at 3 Idealized Ventricular Morphologies. APS, Milwaukee, USA.

Qiu, F., Clark, J.B., Kunselman, A.R., Undar, A., Myers, J.L., 2011. Hemodynamic evaluation of arterial and venous cannulae performance in a simulated neonatal extracorporeal life support circuit. Perfusion 26, 276–283.

Song, X., Wood, H.G., Olsen, D., 2004. Computational fluid dynamics (CFD) study of the 4th generation prototype of a continuous flow ventricular assist device (VAD). Journal of Biomechanical Engineering 126, 180–187.

Tokuda, Y., Song, M.H., Ueda, Y., Usui, A., Akita, T., Yoneyama, S., Maruyama, S., 2008. Three-dimensional numerical simulation of blood flow in the aortic arch during cardiopulmonary bypass. European Journal Cardio-Thoracic Surgery 33, 164–167.

Valen-Sendstad, K., Mardal, K.A., Mortensen, M., Reif, B.A., Langtangen, H.P., 2011. Direct numerical simulation of transitional flow in a patient-specific intracra-nial aneurysm. Journal of Biomechanics 44, 2826–2832.

Vignon-Clementel, I, Figueroa, A, Jansen, K.C.T., 2006. Outflow boundary condi-tions for three-dimensional finite element modeling of blood flow and pressure in arteries. Computer Methods in Applied Mechanics and Engineering 195, 3776–3796.

Wang, Y., Dur, O., Patrick, M.J., Tinney, J.P., Tobita, K., Keller, B.B., Pekkan, K., 2009. Aortic arch morphogenesis and flow modeling in the chick embryo. Annals of Biomedical Engineering 37, 1069–1081.

White, J.K., Jagannath, A., Titus, J., Yoneyama, R., Madsen, J., Agnihotri, A.K., 2009. Funnel-tipped aortic cannula for reduction of atheroemboli. Annals of Thoracic Surgery 88, 551–557.

Yin, W., Alemu, Y., Affeld, K., Jesty, J., Bluestein, D., 2004. Flow-induced platelet activation in bileaflet and monoleaflet mechanical heart valves. Annals of Biomedical Engineering 32, 1058–1066.